POLITECNICO DI TORINO
Repository ISTITUZIONALE

Detection of Hotspots During Domestic Composting by Direct Microwave Imaging Algorithms: A Numerical Assessment

Original
Detection of Hotspots During Domestic Composting by Direct Microwave Imaging Algorithms: A Numerical Assessment / Rodriguez-Duarte, D.O., Masaquiza Caiza, A.R., Shrestha, S., Vipiana, F.. - (2026), pp. 1-5. (20th European Conference on Antennas and Propagation (EuCAP 2026) Dublin (Ire) 19-24 April 2026) [10.23919/eucap68105.2026.11611966].

Availability:
This version is available at: 11583/3016030 since: 2026-09-28T17:43:37Z

Publisher:
Institute of Electrical and Electronics Engineers Inc.

Published
DOI:10.23919/eucap68105.2026.11611966

Terms of use:

This article is made available under terms and conditions as specified in the corresponding bibliographic description in the repository

Publisher copyright
IEEE postprint/Author's Accepted Manuscript

©2026 IEEE. Personal use of this material is permitted. Permission from IEEE must be obtained for all other uses, in any current or future media, including reprinting/republishing this material for advertising or promotional purposes, creating new collecting works, for resale or lists, or reuse of any copyrighted component of this work in other works.

(Article begins on next page)

19 November 2026

Detection of Hotspots During Domestic Composting by Direct Microwave Imaging Algorithms: A Numerical Assessment

David O. Rodriguez-Duarte*, Alex. R Masaquiza-Caiza*, Shreesal Shrestha†, Francesca Vipiana*
*Dept. Electronics and Telecommunications, Politecnico di Torino, Torino, Italy
†School of Computer Science and Engineering, Constructor University, Bremen, Germany
david.rodriguez@polito.it

***Abstract*—Having homogeneous temperature profiles is desirable in composting, especially in low-volume-mass production, a less self-regulated and unstable scenario, where the biomass maturation cycle is more sensitive to the detrimental effects of hotspot disruptions that could annihilate the process. This study numerically assesses the performance of microwave imaging (MWI) as an alternative for detecting these hotspots by using four non-iterative algorithms: truncated singular value decomposition (TSVD) with a Born approximation, delay-and-sum (DAS), multiple signal classification imaging (MUSIC-I), and multifrequency bifocusing (MFBF), and two non-invasive multi-view operation setups, partial and full, to map temperature-related dielectric contrasts within a domestic composter. Overall, the study demonstrates that direct MWI is a feasible approach for compost hotspot detection.**

***Index Terms*—Dielectric characterization, compost processing, inverse scattering, microwave imaging, non-iterative imaging**

I. Introduction

Composting is a naturally occurring exothermic process with variable duration that converts raw organic biomasses, such as agricultural residues or food discards, into a stabilized, sanitized, and humus-like product, the compost [1]. It presents three progressing phases: the mesophilic, thermophilic, and maturation phases, each characterized by distinctive and indicative temperature-defined behavior. In the first phase, microorganisms drive the decomposition of easily degradable organic matter. In the second phase, the temperature rise accelerates the degradation rate while reducing the pathogenic agents in the mass, ensuring its stabilization and sanitation. In the last one, the temperature decreases, and hard-to-degrade molecules are mineralize.

In industrial scenarios, where large volumes of material are used, composting has been refined into a faster, more controlled, and self-regulated process. Conversely, in domestic small-volume ones, the compost mass no longer self-regulates and so more sensitive to sporadic appearing hotspots, which indicate abnormal microbial activity that could critically disrupt and prematurely end the whole process. In this context, the early identification of hotspots without physically disturbing the process is pivotal, though non-trivial. For instance, thermal-optical approaches provide just superficial information, while using temperature sensor(s) gives punctual information within the domain of interest (DoI), risking missing the identification. Besides, it is an invasive approach.

As an alternative, microwave imaging (MWI) offers a non-ionizing, non-invasive, low-intensity, and cost-effective solution capable of generating temperature deviation maps by exploiting the scattering response from the dielectric contrast variation between the overall mass and the hotspots [2]. Indeed, the studied application requires the identification and localization of the hotspots so that one can promptly intervene the process.

Building upon the findings in [2], [3], this work assesses the use and performance of four direct MWI algorithms: truncated singular value decomposition (TSVD) with a Born approximation [4], delay-and-sum (DAS) [5], multiple signal classification imaging (MUSIC-I) [6], and multifrequency bifocusing (MFBF) [7], applied to a 16-antenna cylindrical configuration mimicking a domestic composter. In particular, with the ultimate goal of developing a low-complexity and cost-effective system, we study two multi-view operational configurations that consider either a two-pole-sixteen-through or a two one-pole-eight-through switching modules, which multiplex the transmitters and receptors. Specifically, we use a partial case with a set of eight antennas as transmitters and a different set of eight antennas as receptors, and a full case using sixteen as transceivers. Finally, six imaging metrics are used, including four binary and two full-contrast ones.

II. Mathematical Formulation

MWI is an inverse ill-posed and non-linear problem that retrieves a spatial distribution, i.e., an image, of a dielectric contrast variation, $\Delta\chi$, or a correlated variable, within the DoI. It can be formulated via a scattering problem, with an integral operator casting the contrast accounting for focused thermal variations with the sampled scattered field, as

$$\mathbf{E}_{\text{sct}}(\mathbf{r}_p, \mathbf{r}_q; \omega) = \int_{\text{DoI}} \underline{\mathbf{G}}(\mathbf{r}_p, \mathbf{r}; \omega) \cdot \mathbf{E}(\mathbf{r}, \mathbf{r}_q; \omega) \Delta\chi(\mathbf{r}; \omega) d\mathbf{r}, \tag{1}$$

where $\mathbf{r} \in \text{DoI}$ is the position, $\omega = 2\pi f$ is the angular frequency. $\underline{\mathbf{G}}$ represents the Green's function for an assumed reference scenario, while $\mathbf{E}$ is the total field sampled at the position of the receiver p when transmitting from the position at q. The symbol "$\cdot$" denotes the dot product. This kernel describes the response to a point source as a function of the observation position, forming the point-spread function (PSF), which contains the description of the system [8]. To deal with the inversion, there are two main families of approaches: the direct, non-iterative approach and the iterative approach. In the first case, the algorithm tries to resolve the problem in one shot, avoiding the computational

load burden, which is very convenient when working with applications that require fast results and where qualitative imaging is enough. On the other hand, iterative methods, usually quantitative tomographic ones, retrieve, in addition to the qualitative features, the complex values associated with them, at the price of requiring more computational resources and resolving time, as they work as an iterative optimization problem. In this work, we explore four direct approaches that meet the requirements of the target application.

A. Born Approximation and Truncated Singular Value Decomposition

Assuming "weak" and localized contrast, as in the case of hotspots, the imaging kernel can be linearized using the Born approximation assuming a reference scenario [2], [9]. Then, to invert and regularize the problem, the discretized kernel is decomposed by the singular value decomposition (SVD) in $\langle [u], [\sigma], [v] \rangle$, where σ_n, u_n and v_n are the n-th singular value, right and left singular vectors, respectively, and expressed as

$$\Delta\chi = \sum_{n=1}^{N_T} \frac{1}{\sigma_n} \langle \mathbf{E}_{\text{sct}}, u_n \rangle \, v_n, \tag{2}$$

where N_T is the truncation parameter and acts as a regularizer. To build the kernel, we generate the $\mathbf{E}$ fields using a 2D FEM solver that models a scenario containing the geometric information of the problem, i.e., proves positioning and domain geometry features, as well as the respective dielectric distribution. Since we are interested in an intensity profile, $I(\mathbf{r})$, it is represented like the normalized dielectric contrast, and stated as:

$$I(\mathbf{r}) = \|\Delta\chi\| / \|\Delta\chi\|_{\max}. \tag{3}$$

Moreover, considering in the actual scenario, $\mathbf{E}_{\text{sct}}$ is sampled via the scattering matrix $\mathbf{S} = \mathbf{S}^{t_0} - \mathbf{S}^{t_1}$, where $\mathbf{S}^{t_0}$ and $\mathbf{S}^{t_1}$ represent, respectively, the scattering matrices in two different times, t_0 and t_1, a calibration using a known scenario is used to convert and conveniently scale the measured scattering parameters [10], [11] (here obtained via a 3D full-wave simulation, see Sect. III).

B. Delay-And-Sum

The DAS is a confocal-based imaging algorithm used in several applications due to its robustness and computational efficiency [5]. It applies propagation-path-based delays to the collected data, which are then coherently summed to produce an intensity map. Regions that exhibit significant contrast correspond to discontinuities. MWI reconstructions are commonly degraded by clutter and unwanted early- and late-time responses, which can mask the responses of interest. To remove these non-desired responses, clutter, a straightforward differential approach is used, subtracting the temporal reflection response of each i-antenna at t_0 from a the response at t_1, $\Delta\mathcal{M}_i = \mathcal{M}_i^{t_0} - \mathcal{M}_i^{t_1}$. With the unchanged system geometry and acquisition setup, the clutter is removed, so $\Delta\mathcal{M}_i$ reflects the temporal changes. The intensity profile $I(\mathbf{r})$ at any focal point $\mathbf{r}$ within the DoI is computed as:

$$I(\mathbf{r}) = \sum_{i=1}^{N} \Delta\mathcal{M}_i(\tau_i(\mathbf{r})), \tag{4}$$

where $\tau_i(\mathbf{r}) = 2\|\mathbf{r} - \mathbf{r}_i\|/v$ represents the signal's travel delay from the i-transmitter's phase center $\mathbf{r}_i$ to any focal point $\mathbf{r}$ in the DoI, and v denotes the wave propagation velocity in the background medium, and N the number of antennas.

C. Multifrequency Bifocusing

In this case, the $I(\mathbf{r})$ is obtained by coherently summing the contributions from all transmitter-receiver pairs across all frequencies is calculated as in [7]:

$$I(\mathbf{r}) = \sum_{f} \sum_{i=1}^{N_{\text{TX}}} \sum_{j=1}^{N_{\text{RX}}} \mathbf{E}_{\text{sct}}^{ji}(f) \cdot \underline{\mathbf{G}}(\mathbf{r}, \mathbf{r}_{\text{TX}^i}, f) \cdot \underline{\mathbf{G}}(\mathbf{r}, \mathbf{r}_{\text{RX}^j}, f), \tag{5}$$

where $\mathbf{E}_{\text{sct}}^{ji}(f)$ represents the scattered electric field corresponding to transmitter-receiver pair (i, j) at frequency f. N_{TX} and N_{RX} indicate the total number of transmitters and receivers, respectively, and $\underline{\mathbf{G}}$ is the back-propagation Green's function that focuses the field from the source position $\mathbf{r}_{\text{src}}$ to $\mathbf{r}$, which can be defined for two-dimensional problems as:

$$\underline{\mathbf{G}}(\mathbf{r}, \mathbf{r}_{\text{src}}, f) = \sqrt{||\mathbf{r} - \mathbf{r}_{\text{src}}||} \cdot e^{+jk(f)||\mathbf{r} - \mathbf{r}_{\text{src}}||}, \tag{6}$$

where $||\mathbf{r} - \mathbf{r}_{\text{src}}|| = \sqrt{(x - x_{\text{src}})^2 + (y - y_{\text{src}})^2}$ is the Euclidean distance. The wavenumber $k(f)$ is frequency-dependent and defined as:

$$k(f) = \frac{2\pi f}{c_0} \sqrt{\varepsilon_{\text{r}_b}}. \tag{7}$$

Here, c_0 is the speed of light in vacuum and ε_{r_b} is the relative permittivity of the background medium.

D. Multiple Signal Classification Imaging

The MUSIC-I is a subspace-based method that achieves high spatial resolution by exploiting the eigenstructure of the data covariance matrix [6]. For each frequency point f, the SVD of $\mathbf{S}$ is performed as:

$$\mathbf{S}(f) = \sum_{m=1}^{N_F} \sigma_m(f) u_m(f) v_m^*(f) \approx \sum_{m=1}^{M_T} \sigma_m(f) u_m(f) v_m^*(f). \tag{8}$$

Then, the M_T dominant eigenvectors of the total N_F are projected onto the noise subspace as:

$$\mathbf{P}_{noise}(f) = \mathbf{I}_N - \sum_{m=1}^{M_T} u_m(f) u_m^*(f), \tag{9}$$

where $\mathbf{I}_N$ denotes the $N \times N$ identity matrix. To form the intensity map, a model of wave propagation between the antennas and each point $\mathbf{r}$ in the imaging domain is needed, thus a steering vector $\mathbf{w}(\mathbf{r}, f)$ is defined as:

$$\mathbf{w}(\mathbf{r}, f) = \begin{bmatrix} e^{-jk(f)\|\mathbf{r} - \mathbf{r}_1\|} \\ e^{-jk(f)\|\mathbf{r} - \mathbf{r}_2\|} \\ \vdots \\ e^{-jk(f)\|\mathbf{r} - \mathbf{r}_N\|} \end{bmatrix} \tag{10}$$

Finally, the intensity map $I(\mathbf{r})$ is obtained by summing contributions across all frequency points. This pseudo-spectrum exhibits sharp peaks at the positions of the scatterers, as the steering vector $\mathbf{w}(\mathbf{r}, f)$ is almost orthogonal to the noise

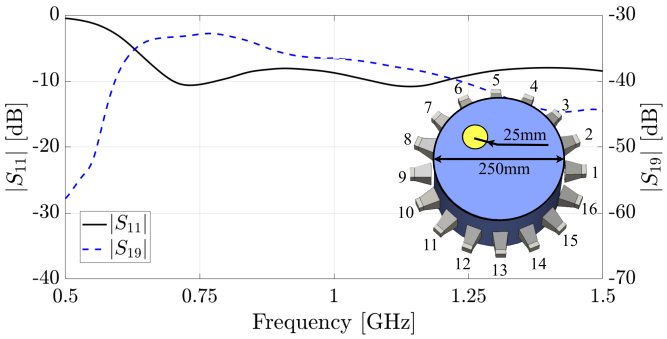


Fig. 1. Simulated scattering parameters, $|S_{11}|$ and $|S_{19}|$, for the 16-antenna circular array with a geometry schematic and dimensions included in the bottom-right corner scheme. Permittivity values based on [3].

subspace. This characteristic allows the MUSIC-I algorithm to achieve super-resolution imaging.

$$I(\mathbf{r}) = \frac{1}{\sum_{f} \left\| \mathbf{P}_{\text{noise}}(f) \left[\mathbf{w}(\mathbf{r}, f) \right] \right\|^2} \tag{11}$$

III. Validation

A. Numerical Setup

To evaluate the performance of the aforementioned inversion algorithms, we generate synthetic 'input 'measure" scattering data for all algorithms by full-wave simulating a MWI system consisting of 16 horn antennas evenly spaced around a cylindrical container with the dimension of a domestic composter as illustrated in Fig. 1, and in agreement with the feasibility proofing in [2]. The baseline mass and the hotspot dielectric properties are set according to the values reported in [3], and indicate a drift of about 4 °C. Moreover, to build the TSVD imaging kernel and calibrate the input data, we employ an in-house 2D EM finite element method (FEM) solver. The reconstructions for the full- and partial-multiplexing configuration are shown in Figs. 3 and 4, respectively. In these, and in subsequent metrics, the Born approximation with the truncated SVD, is dubbed as S-F TSVD, in the single frequency case and as M-F TSVD in the multi-frequency one. To build the kernel, we consider 1 GHz for the former, and [0.5 1.0 1.5] GHz for the latter. The other algorithms use the data from the whole band, $0.5 - 1.5$ GHz. Qualitative assessment of the retrieved intensity maps indicates that the hotspot region is generally well-identified in the baseline composting mass. The results also suggest a trade-off between system complexity, implementation costs, and image fidelity. Either multiplexing setup can be practically implemented using commercially available switches, such as the 2x64 channel electronic correlator [12] for full- and partial-multiplexing, and the 1x8 channel solid-state switch [13] for partial-multiplexing.

B. Performance

The performance of MWI algorithms is assessed using six image-quality metrics: four binary metrics and two full-contrast metrics. The binary-based ones include: Intersection over Union (IoU) to measure the spatial precision in terms of the overlap between the reconstructed target and the corresponding ground truth; Dice Similarity Coefficient (DSC) [14] to evaluate the similarity of the two binary segmentations; a Size-based metric (S-BM) and a Boundary-based metric (B-BM), both introduced in [15], to evaluate how closely the reconstructed target size and the mismatch in the boundaries alignment corresponds with ground truth, respectively. The full contrast metrics include Structural Similarity Index (SSIM) [16] to evaluate the perceptual similarity between the reconstruction and ground truth, and the Contrast-to-Noise Ratio (CNR) [17] to measure how well the target stands out from the background. The first five metrics range from 0 to 1, with 1 indicating complete similarity and 0 no similarity between the binarized reconstruction with the corresponding ground truth. In contrast, CNR is unbounded, and high CNR values suggest improved target visibility in the reconstructed image. Here, it is worth noticing that we do not apply noise, and the apparent distortions are actually intrinsic imaging artifacts. Table I summarizes the results for both multiplexing setups. In full-multiplexing, all inversion algorithms accurately identify and locate the hotspot. MUSIC-I has lower overall performance across the

TABLE I
Performance Metrics of Full Multiplexing Configuration

Metric	S-F TSVD	M-F TSVD	MFBF	MUSIC-I	DAS
Full-multiplexing configuration					
IoU	0.5669	0.5327	0.7263	0.0765	0.7872
DSC	0.7236	0.6952	0.8415	0.1421	0.8810
S-BM	0.7739	0.6952	0.9798	0.1421	0.9881
B-BM	0.1960	0.8489	0.9026	0.5419	0.9090
SSIM	0.0945	0.1217	0.0098	0.9329	0.0088
CNR	2.5485	2.7687	3.2875	0.7145	2.226
Partial-multiplexing configuration					
IoU	0.1213	0.5455	0.5727	0.0647	0.3129
DSC	0.2258	0.7059	0.7283	0.1215	0.4767
S-BM	0.9839	0.9748	0.9524	0.1215	0.5475
B-BM	0	0.0249	0.1045	0.6048	0
SSIM	0.0326	0.0934	0.0069	0.0419	0.0069
CNR	0.6643	2.3531	2.3085	0.8901	2.14

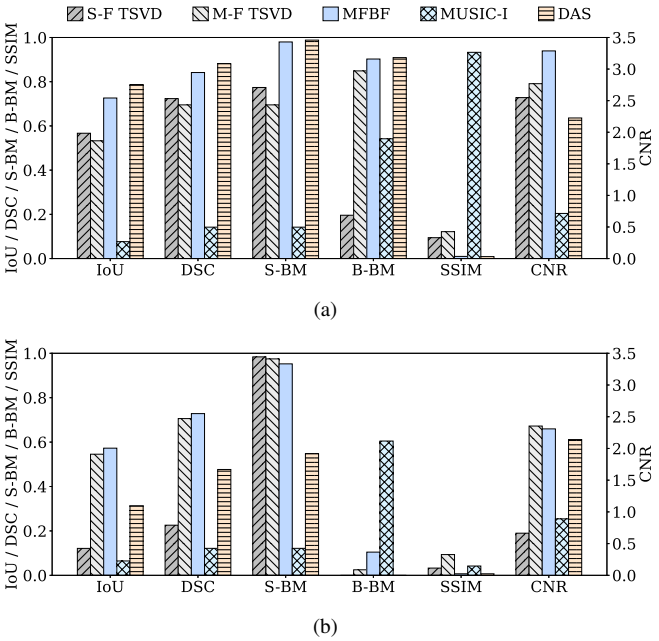


Fig. 2. Performance metrics of (a) full-multiplexing and (b) partial-multiplexing configuration

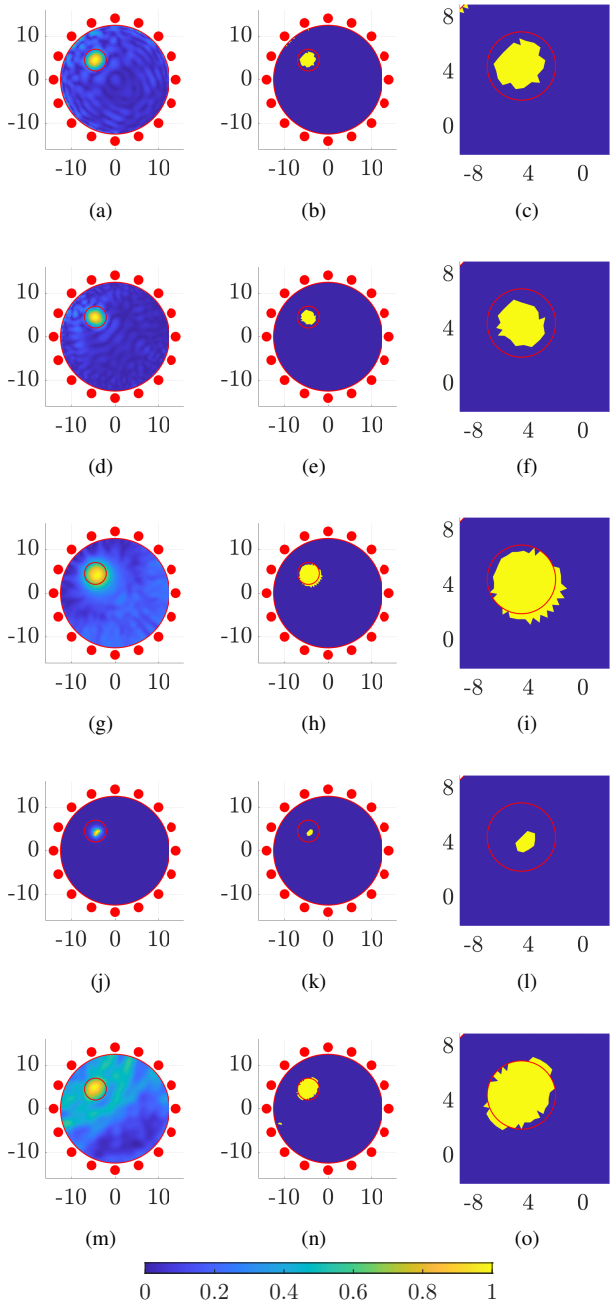


Fig. 3. Normalized reconstructions for the full-multiplexing configuration using different MWI algorithms (a-c) S-F TSVD, @1GHz; (d-f) M-F TSVD; (g-i) MFBF; (j-l) MUSIC-I; (m-o) DAS. Each row shows: (left) normalized reconstruction; (middle) binary mask by thresholding the reconstruction at 0.563 ($\approx$ 5 dB); (right) a zoom-view of the target region. Dimensions in [cm]. The internal red contour outline the hotspot area. The red points indicate the positions of the phase center of the transceiver elements.

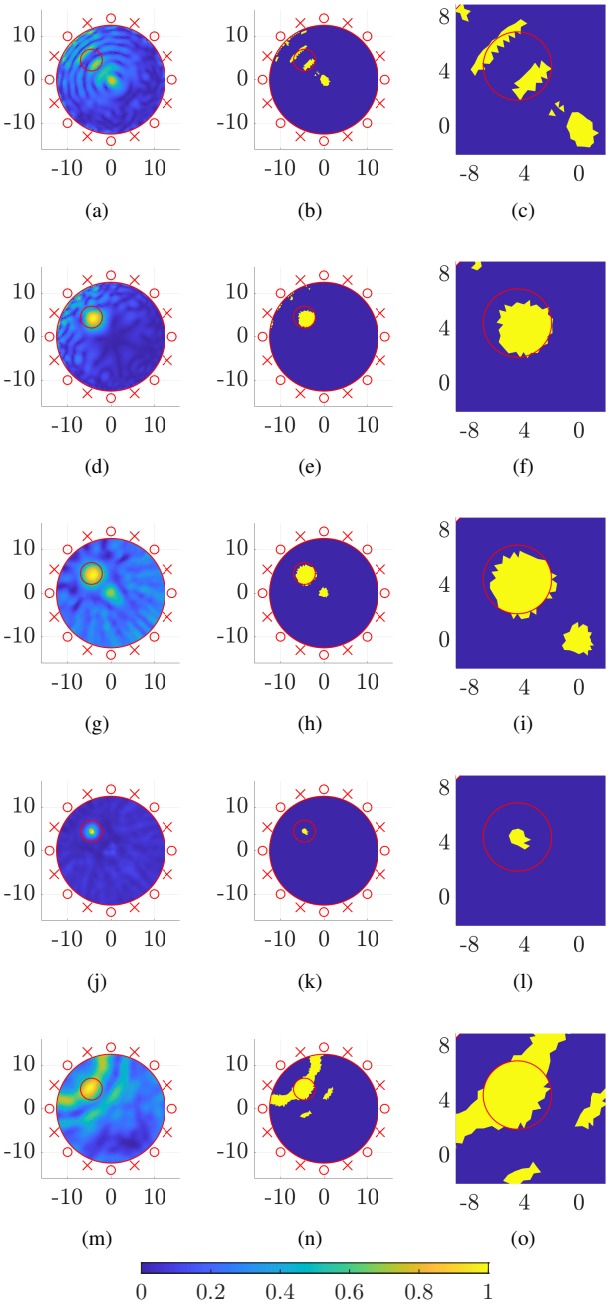


Fig. 4. Normalized reconstructions for the partial-multiplexing configuration using different MWI algorithms. (a-c) S-F TSVD, @1GHz; (d-f) M-F TSVD; (g-i) MFBF; (j-l) MUSIC-I; (m-o) DAS. Each row shows: (left) normalized reconstruction; (middle) binary mask by thresholding the reconstruction at 0.563 ($\approx$ 5dB); (right) a zoom-view of the target region. Dimensions in [cm]. The internal red contour outline the hotspot area. The red crosses indicate the positions of the phase center of the transmitters, while the circles indicates the receivers.

binary-based metrics, it generates very localized contrast peaks that, when thresholded, produce punctual targets. But it achieves the highest SSIM due to reduced background distortions. MFBF and DAS have lower SSIM values due to significant background distortions as shown in Fig. 3. CNR is comparable across most algorithms except for MUSIC-I. In partial-multiplexing, M-F TSVD and MFBF have in general good performance across some metrics, followed by DAS, MUSIC-I, and S-F TSVD. In this configuration, it is more evident that all algorithms introduce distortions that reduce the B-BM score, which is very sensitive to artifacts present in the binarized reconstructions. MUSIC-I, in contrast, does not introduce artifacts, and thus exhibits good B-BM score. SSIM values are lower for all algorithms in this setup. Overall, the quantitative analysis confirms that MWI effectively identifies and localizes hot spots using both full- and partial-multiplexing configurations. S-F TSVD shows higher distortion in partial multiplexing, confirming the need for multi-frequency approaches. Finally, for the sake of clarity and easier comparison, Fig. 2 illustrates the metrics.

IV. Conclusion and Perspective

This paper assessed different non-iterative MWI algorithms, expressed in their 2D version, for detecting harmful hotspots that appear during domestic composting, where the composter is modeled as a cylindrical container. Only a single hotspot was considered in this analysis, although multiple hotspots may occur in the compost mass. Though this simplified scenario, it is still meaningful as it provides valuable learnings, more narrowly framed, that can be extrapolated to more complex ones. Starting with a mathematical generalization, the hotspot detection is stated as an imaging problem aimed at retrieving an intensity map. The results show MWI is a good alternative for detection, regardless of the approach used. However, the imaging performance might act as a driving design tool.

In future work, we expect to extend the presented analysis to 3D formulations and more realistic scenarios, as well as experimentally validate the results.

V. Acknowledgment

This study was carried out within the Agritech National Research Center and received funding from the European Union Next-GenerationEU (PIANO NAZIONALE DI RIPRESA E RESILIENZA (PNRR) – MISSIONE 4 COMPONENTE 2, INVESTIMENTO 1.4 – D.D. 1032 17/06/2022, CN00000022), and by the research project "3BAtwin" funded by Horizon EU FP (GA: 101159623). This is also part of DAAD Research Internships in Science and Engineering (RISE) Worldwide Scholarship, funded by the German Federal Foreign Office.

References

[1] R. Harrison, "Composting and Formation of Humic Substances," in *Encyclopedia of Ecology*, S. E. Jørgensen and B. D. Fath, Eds. Oxford: Academic Press, 2008, pp. 713–719.

[2] D. O. Rodriguez-Duarte, M. Fiore, A. De Simone, F. Riente, G. Turvani, F. Demichelis, T. Tommasi, and F. Vipiana, "A Feasibility Study on Microwave Imaging for Domestic Compost Production Monitoring," in *2024 IEEE International Workshop on Metrology for Agriculture and Forestry (MetroAgriFor)*, 2024, pp. 586–591.

[3] D. O. Rodriguez-Duarte, M. Fiore, F. Riente, G. Turvani, F. Demichelis, T. Tommasi, and F. Vipiana, "Broadband Dielectric Characterization of Manure and Compost," in *2024 IEEE 1st Latin American Conference on Antennas and Propagation (LACAP)*, 2024, pp. 1–2.

[4] M. Bertero, P. Boccacci, and C. De Mol, *Introduction to inverse problems in imaging*. CRC press, 2021.

[5] E. Fear, X. Li, S. Hagness, and M. Stuchly, "Confocal microwave imaging for breast cancer detection: localization of tumors in three dimensions," *IEEE Transactions on Biomedical Engineering*, vol. 49, no. 8, pp. 812–822, 2002.

[6] W.-K. Park and D. Lesselier, "Electromagnetic MUSIC-type imaging of perfectly conducting, arc-like cracks at single frequency," *Journal of Computational Physics*, vol. 228, no. 21, pp. 8093–8111, 2009.

[7] L. Jofre, A. P. Toda, J. M. J. Montana, P. C. Carrascosa, J. Romeu, S. Blanch, and A. Cardama, "UWB Short-Range Bifocusing Tomographic Imaging," *IEEE Transactions on Instrumentation and Measurement*, vol. 57, no. 11, pp. 2414–2420, 2008.

[8] N. K. Nikolova, *Introduction to microwave imaging*. Cambridge University Press, 2017.

[9] D. O. Rodriguez-Duarte, C. Origlia, J. A. T. Vasquez, R. Scapaticci, L. Crocco, and F. Vipiana, "Experimental assessment of real-time brain stroke monitoring via a microwave imaging scanner," *IEEE Open Journal of Antennas and Propagation*, vol. 3, pp. 824–835, 2022.

[10] C. Gilmore, P. Mojabi, A. Zakaria, M. Ostadrahimi, C. Kaye, S. Noghanian, L. Shafai, S. Pistorius, and J. LoVetri, "A Wideband Microwave Tomography System With a Novel Frequency Selection Procedure," *IEEE Transactions on Biomedical Engineering*, vol. 57, no. 4, pp. 894–904, 2010.

[11] Z. Miao, P. Kosmas, and S. Ahsan, "Impact of information loss on reconstruction quality in microwave tomography for medical imaging," *Diagnostics*, vol. 8, no. 3, p. 52, 2018.

[12] E. Technologies, *EVT1064-EVT3064 Datasheet*, EV Technologies, Oct 2025, accessed: Oct. 17, 2025. [Online]. Available: https://ev-technologies.com/portfolio-items/smart-rf-mmwave-correlators/

[13] Mini-Circuits, *SP8T Solid-State Switch Module USB-1SP8T-852H*, Mini-Circuits, Oct 2025, accessed: Oct. 17, 2025. [Online]. Available: https://www.minicircuits.com/pdfs/USB-1SP8T-852H.pdf

[14] V. Thada and V. Jaglan, "Comparison of jaccard, dice, cosine similarity coefficient to find best fitness value for web retrieved documents using genetic algorithm," *International Journal of Innovations in Engineering and Technology*, vol. 2, no. 4, pp. 202–205, 2013.

[15] F. Xue, L. Guo, A. Bialkowski, and A. M. Abbosh, "Integrated Boundary-Overlap-Size Metric for Local Assessment of Deep Learning Methods in Medical Microwave Imaging," *IEEE Journal of Electromagnetics, RF and Microwaves in Medicine and Biology*, vol. 9, no. 2, pp. 229–239, 2025.

[16] Z. Wang, A. Bovik, H. Sheikh, and E. Simoncelli, "Image quality assessment: from error visibility to structural similarity," *IEEE Transactions on Image Processing*, vol. 13, no. 4, pp. 600–612, 2004.

[17] X. Song, B. W. Pogue, S. Jiang, M. M. Doyley, H. Dehghani, T. D. Tosteson, and K. D. Paulsen, "Automated region detection based on the contrast-to-noise ratio in near-infrared tomography," *Applied optics*, vol. 43, no. 5, pp. 1053–1062, 2004.